MRI monitoring of temperature and displacement for transcranial focus ultrasound applications

Valéry Ozenne, Charlotte Constans, Pierre Bour, Mathieu Santin, Romain Valabrègue, Harry Ahnine, Pierre Pouget, Stephane Lehéricy, Jean-François Aubry, B. Quesson

NeuroImage 204 (2020) 116236

Contents lists available at ScienceDirect

NeuroImage

journal homepage: www.elsevier.com/locate/neuroimage

MRI monitoring of temperature and displacement for transcranial focus ultrasound applications

Valéry Ozenne [a,b,c,*], Charlotte Constans [d], Pierre Bour [a,b,c], Mathieu D. Santin [e,f], Romain Valabrègue [e,f], Harry Ahnine [e], Pierre Pouget [e], Stephane Lehéricy [e,f], Jean-François Aubry [d,1], Bruno Quesson [a,b,c,1]

[a] IHU Liryc, Electrophysiology and Heart Modeling Institute, Fondation Bordeaux Université, Bordeaux, France
[b] Univ. Bordeaux, Centre de Recherche Cardio-Thoracique de Bordeaux, U1045, Bordeaux, France
[c] INSERM, Centre de Recherche Cardio-Thoracique de Bordeaux, U1045, Bordeaux, France
[d] Physics for Medicine Paris, Inserm, ESPCI Paris, CNRS, PSL Research University, Univ Paris Diderot, Sorbonne Paris Cité, Paris, 75012, France
[e] Institut du Cerveau et de la Moelle épinière - ICM, Sorbonne Université, Inserm U 1127, CNRS UMR, Paris, 7225, France
[f] Institut du Cerveau et de la Moelle épinière, Centre de NeuroImagerie de Recherche - CENIR, Paris, France

ARTICLE INFO

Keywords:
Magnetic resonance guided high intensity focused ultrasound
Acoustic radiation force imaging
Magnetic resonance thermometry
Proton resonance frequency shift
Brain imaging

ABSTRACT

Background: Transcranial focus ultrasound applications applied under MRI-guidance benefit from unrivaled monitoring capabilities, allowing the recording of real-time anatomical information and biomarkers like the temperature rise and/or displacement induced by the acoustic radiation force. Having both of these measurements could allow for better targeting of brain structures, with improved therapy monitoring and safety.

Method: We investigated the use of a novel MRI-pulse sequence described previously in Bour et al., (2017) to quantify both the displacement and temperature changes under various ultrasound sonication conditions and in different regions of the brain. The method was evaluated in vivo in a non-human primate under anesthesia using a single-element transducer (f = 850 kHz) in a setting that could mimic clinical applications. Acquisition was performed at 3 T on a clinical imaging system using a modified single-shot gradient echo EPI sequence integrating a bipolar motion-sensitive encoding gradient. Four slices were acquired sequentially perpendicularly or axially to the direction of the ultrasound beam with a 1-Hz update frequency and an isotropic spatial resolution of 2-mm. A total of twenty-four acquisitions were performed in three different sets of experiments. Measurement uncertainty of the sequence was investigated under different acoustic power deposition and in different regions of the brain. Acoustic simulation and thermal modeling were performed and compared to experimental data.

Results: The sequence simultaneously provides relevant information about the focal spot location and visualization of heating of brain structures: 1) The sequence localized the acoustic focus both along as well as perpendicular to the ultrasound direction. Tissue displacements ranged from 1 to 2 μm. 2) Thermal rise was only observed at the vicinity of the skull. Temperature increase ranged between 1 and 2 °C and was observed delayed relative the sonication due to thermal diffusion. 3) The fast frame rate imaging was able to highlight magnetic susceptibility artifacts related to breathing, for the most caudal slices. We demonstrated that respiratory triggering successfully restored the sensitivity of the method (from 0.7 μm to 0.2 μm). 4) These results were corroborated by acoustic simulations.

Conclusions: The current rapid, multi-slice acquisition and real-time implementation of temperature and displacement visualization may be useful in clinical practices. It may help defining operational safety margins, improving therapy precision and efficacy. Simulations were in good agreement with experimental data and may thus be used prior treatment for procedure planning.

* Corresponding author. Electrophysiology and Heart Modeling Institute, Hopital Xavier Arnozan, Avenue du Haut Lévêque, Pessac, 33600, France
E-mail addresses: valery.ozenne@u-bordeaux.fr (V. Ozenne), charlotte.constans@gmail.com (C. Constans), pierre.bour@ihu-liryc.fr (P. Bour), mathieu.santin@icm-institute.org (M.D. Santin), romain.valabregue@upmc.fr (R. Valabrègue), harry.ahnine@gmail.com (H. Ahnine), pierre.pouget@upmc.fr (P. Pouget), stephane.lehericy@upmc.fr (S. Lehéricy), jean-francois.aubry@espci.fr (J.-F. Aubry), bruno.quesson@u-bordeaux.fr (B. Quesson).
[1] These authors contributed equally to this work.

https://doi.org/10.1016/j.neuroimage.2019.116236
Received 22 May 2019; Received in revised form 27 September 2019; Accepted 28 September 2019
Available online 6 October 2019

1. Introduction

MR-guided High Intensity Focused Ultrasound (MRgHIFU) is gaining popularity in functional neurosurgery with the recent success of non-invasive thalamotomy for essential tremor (Lipsman et al., 2013; Martinez-Fernandez et al., 2018). Other therapeutic applications are under investigation such as the treatment of Parkinson's disease (Martinez-Fernandez et al., 2018), chronic pain (Jeanmonod et al., 2012) or Alzheimer 's disease (Lipsman et al., 2018). In neuroscience, transient neuromodulation by transcranial ultrasonic stimulation (TUS) has been demonstrated in rodents (Tufail et al., 2011; Yang et al., 2012; Younan et al., 2013; Ye et al., 2016; Kamimura et al., 2016), in non-human primates (NHP) (Wattiez et al., 2017; Deffieux et al., 2013), and more recently in humans (Legon et al., 2014; Lee et al., 2016a). For both MRgHIFU and TUS applications, accurate targeting and monitoring are crucial. MRgHIFU treatment relies on local thermal tissue damage (Elias et al., 2013; Huang et al., 2018), whereas mechanical effects are considered to play a major role in TUS (Plaksin et al., 2014; Naor et al., 2016). In both applications, the ability to visualize thermal elevation at the focus or in specific regions of the brain is essential for the safety of the procedure.

Under MRI, temperature can be mapped in brain structures using the Proton Resonance Frequency Shift (PRFS) thermometry (Peters et al., 1998). Micrometric tissue displacement resulting from the acoustic radiation force pressure can be mapped by MR Acoustic Radiation Force Imaging (MR-ARFI). MR-ARFI has been proposed initially to identify the focal point location before starting the therapy (Marsac et al., 2012). Clinical translation of MR-ARFI imaging is restricted by technological difficulties of implementing such methods in current clinical treatment systems. Except for the work reported by Hertzberg et al. (2010), most studies (Bitton and Pauly, 2014; de Bever et al., 2018; Kaye et al., 2011; Paquin et al., 2013; Odeen et al., 2018) were performed in phantom or in ex vivo brain tissue. Direct application of these studies in in vivo settings remains uncertain, and may be compromised by physiological noise or potential restrictions in the placement of MRI coil elements due to the HIFU device.

In vivo evaluation of MR-ARFI in brain has recently been reported by Gaur et al. (2018) and Jonathan et al. (2018). Although these studies showed promising preliminary results regarding accuracy of the focal spot localization, no data have yet been reported simultaneously quantifying potential heating of the brain. Yet, the associated total acoustic energy deposition may lead to substantial temperature exposure of brain structures. Different options have been proposed either to reduce or to monitor such potential unwanted heating. For instance, Zheng et al. (2018) published a highly sensitive method based on steady state free precession technique that minimized sonication duration to 1.45 ms and thus the potential heating. Other approaches consist to monitor MR-ARFI and temperature at the same time (de Bever et al., 2018; Bour et al., 2017; Mougenot et al., 2016). An optimal MRI monitoring method should provide high sensitivity to both focal spot temperature and displacement simultaneously, while ensuring important volumetric coverage to visualize the effects of HIFU over the full ultrasound path. It should also provide high spatial and temporal resolutions and reduced acoustic energy deposition.

In this work, we evaluate in an alive NHP a simultaneous MR-ARFI-thermometry (MR-ARFI-THERMO) sequence (Bour et al., 2017) implemented at 3T. This sequence allows sub second multi-slice temperature and displacement imaging during sonication with a temporal resolution of 75 ms per slice at an isotropic spatial resolution of 2-mm. The monitoring capabilities of the sequence were evaluated under different acoustic power depositions and the impact of physiological noise was quantified in two different areas of the brain. Finally, experimental temperature and displacement results were compared with validated (Constans et al., 2017) modeling of ultrasound propagation through the skull and into the brain.

2. Method

2.1. MRI and focused ultrasound sonication

All acquisitions were performed on a 3T clinical imaging system (MAGNETOM Prisma, Siemens Healthcare, Erlangen, Germany) using a modified single-shot gradient echo EPI with repeated acquisitions (Fig. 1A). At each time frame, the sequence integrated a bipolar motion-sensitive encoding gradient (MEG) with an alternated polarity between two successive acquisitions (Fig. 1B). The focal displacement could be encoded in either longitudinal or transverse planes using a MEG with direction aligned along slice or phase encoding direction, respectively. The raw data were streamed in real-time to a separate workstation and the images were reconstructed online using the Gadgetron framework (Hansen and Sorensen, 2013). The resulting images were streamed back to the MR database and to a separate computer for display. The average displacement and temperature values were then computed in Thermoguide™ software (Image Guided Therapy SA, Pessac, France) from online reconstructed phase images ϕ_i by summing and subtracting two consecutive phase images:

$$\Delta T_i = \frac{\left(\phi_i^+ - \phi_{ref}^+\right) + \left(\phi_{i-1}^- - \phi_{ref}^-\right)}{(2.\gamma.\alpha.TE.B0)} \quad [1]$$

$$\Delta D_i = (-1)^i \frac{\left(\left(\phi_i^+ - \phi_{ref}^+\right) - \left(\phi_{i-1}^- - \phi_{ref}^-\right)\right)}{(2.\gamma.|A|.\Delta)} \quad [2]$$

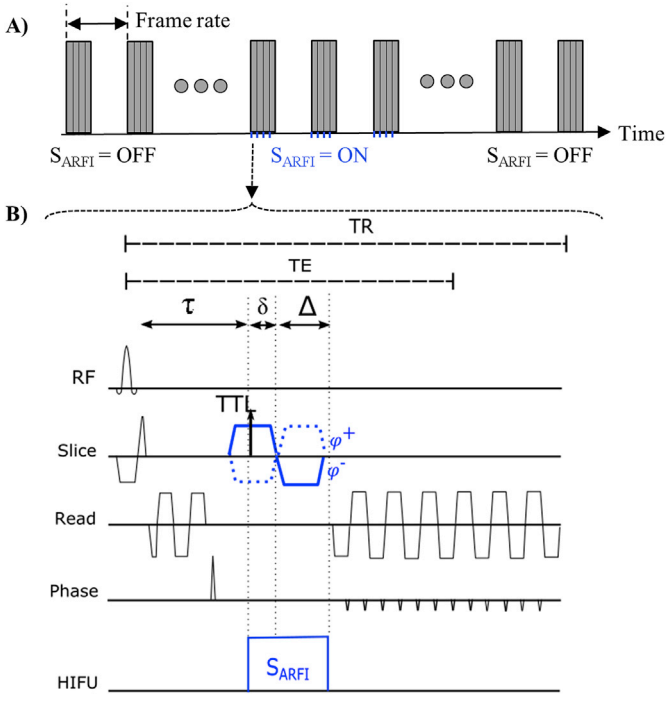

Fig. 1. Description of the MR-ARFI-THERMO method. A) Four slices were acquired sequentially with a fixed frame rate (typically 0.5 or 1 Hz) or respiratory gating. The focus ultrasound sonication was triggered from the MRI sequence by a TTL. Sonication was turned on during between 10 and 30 dynamic acquisitions. B) Schematic of the single-shot echo planar imaging MR-ARFI-thermometry sequence integrating MEG (in blue) with alternating polarities (ϕ^+ and ϕ^-) to encode both temperature and ARFI displacement in the phase of the reconstructed MR image. Ultrasound sonications (S_{ARFI}) are represented in the bottom line in blue. The TTL arrow indicates the timing of the output synchronization signal from the MR acquisition sequence used for triggering the (S_{ARFI}) pulse of the HIFU generator. δ and Δ respectively represent the adjustable offset of the TTL signal relative to the beginning of the second lobe of the MEG gradient and the duration of this lobe.

In this technique, ϕ_i and ϕ_{i-1} refer to two consecutive phase images in time and $\phi_i^{+/-}$ are reference phase images acquired prior to the acoustic sonication. $\delta = 267.522\,10^6$ rad s^{-1}.T^{-1} is the gyromagnetic ratio, $\alpha = -0.0094$ ppm °C^{-1} is the PRFS constant, TE is the echo time, B0 = 2.89 T is the static magnetic induction. Δ is the duration of the MEG, and A its amplitude. To enhance the displacement sensitivity of the sequence, we used a high gradient amplitude of A = 54 mT/m. The flat top MEG duration (Δ) was set to 5 ms with 1 ms ramp times. For a detailed description of the method and its implementation, please refer to (Bour et al., 2017).

Sonications were performed using a single-element transducer (H115, Sonic Concepts, Bothel, USA, focal length 63 mm, aperture 64 mm) that was operated at 850 kHz. The transducer was driven by a RF-generator (75A250, Amplifier Research, Souderton, USA). Custom made low pass filters were introduced in the transmission line to prevent electromagnetic artifacts on MR images during sonication. The sonication was triggered from the MRI sequence (see Fig. 1) by a TTL signal that could be generated with configurable timing during the MEG. An offset of −2 ms before the second lobe was set to leave enough time to the brain tissue to reach a steady state displacement due to tissue viscoelasticity (Larrat et al., 2009). The sonication duration of S_{ARFI} ranged between 4 and 8 ms with adjustable amplitude.

2.2. Animal preparation

In vivo evaluation of the method was performed in the brain of an adult NHP (Macaca Mulatta). The animal was placed in the foot-head direction in the magnet using a dedicated MRI chair (Rogue Research) after positioning the transducer near the head using a mechanical holder. Acoustic coupling of the transducer with the head was achieved by a water-filled inflatable balloon (Fig. 2). After positioning of the animal at the magnet isocenter, MRI data were acquired with two antennas with four receive elements surrounding the head. The animal was maintained under general anesthesia with a blend of isoflurane (0.8%) and oxygen (1∼2L/mn). ECG and arterial pressure were monitored continuously during the procedure.

Experimental Protocol: The procedure followed these steps:

- Localization of the transducer relative to the brain was done using a MP-RAGE sequence acquired at 1 mm isotropic resolution, with TE/TR/TI/FA = 2.28 ms/2300 ms/920 ms/9°, bandwidth = 200 Hz/px, GRAPPA = 2, matrix size = 256*256 × 256, FOV = 256 × 256 × 256 mm^3. After completion of the acquisition (∼5min), positioning of the MR-ARFI slices on the target region was prepared using the 3D rendering console of the MR vendor by considering a focal length of 63 mm.
- MR-ARFI-thermometry acquisition: Image orientation was set either perpendicular (MEG set in the slice direction) or parallel (MEG set in the phase direction) to the propagation axis of the ultrasound beam. Four slices were acquired sequentially (Fig. 1A) with an adjustable number of repetitions (at least 30) using either a fixed repetition time (1 s or 2 s) or respiratory gating (see Table 2 in supplementary materials). The respiratory gating was used to evaluate the influence of respiration on the accuracy of the displacement estimate in voxels at different locations in the brain. The first repetitions were used to generate the reference phase images for both MEG polarities before HIFU shots were applied during the subsequent acquisitions. Acquisition parameters were: a FOV of 189 × 189 mm^2, a 96 × 96 matrix size, 2 mm slice thickness, leading to an isotropic resolution of 2 mm and 2 mm slice gap. TE/TR/FA = 29 ms/300 ms/60°, with a minimal repetition time/slice of 75 ms. GRAPPA acceleration of 2, 6/8 partial Fourier, bandwidth = 1565 Hz/voxel, ETL = 25.92 ms, echo spacing = 0.72 ms.

2.3. Data analysis

Twenty-four MR-ARFI-THERMO acquisitions were performed in three different experiments on different days in the same animal. For each acquisition, the measurement uncertainty was evaluated by computing the temporal standard deviation (σ) and temporal mean (μ) for both displacement (D) and temperature (T) over 10 successive dynamic acquisitions selected before, during and after S_{ARFI} sonication. Negative values of the baseline displacement were corrected by adding an offset in order to reach a baseline value equal to zero. The temporal mean of the displacements (μ_D) was fitted to a two-dimensional Gaussian function from which the maximum amplitude, focus location and full width at half maximum (FWHM) were extracted.

2.4. Acoustic simulations

The simulations were performed using k-Wave, a k-space pseudo-spectral method-based solver (Cox et al., 2007). The transducer was modeled as a spherical section (63 mm radius of curvature and 64 mm active diameter). Several simulations were performed with varying pulse length to reflect the durations used experimentally (4 ms–8 ms). The transducer was spatially apodized (r = 0.35) on the spherical section and

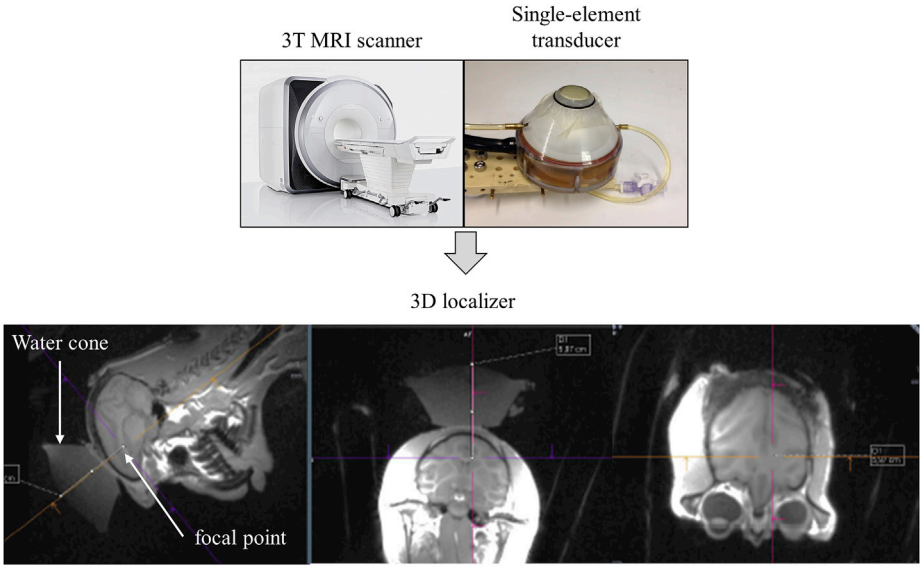

Fig. 2. Presentation of the set up. MR data were acquired at 3T using two 4-element receive coil positioned laterally to the head. A single-elements phase array transducer was operated at 850 kHz. Acoustic coupling of the transducer with the head was achieved by a water-filled inflatable balloon as shown in the picture. Images on the bottom display 3 orthogonal views reformatted from the 3D MP-RAGE acquisition. The water cone and the expected location of the focal point are indicated (white arrows).

the emission frequency was set to 850 kHz. For calibration purposes, the simulations were first performed in water and compared with the pressure values measured experimentally with a heterodyne interferometer (Constans et al., 2017). The efficiency of the transducer was modeled in the simulation by using these measurements to apply a linear scaling factor such that the simulated and measured peak negative pressures were brought into agreement.

Simulation were then performed, modeling the propagation of focused ultrasound in the NHP's head to predict the pressure field in the brain (Fig. 3). To avoid factors contributing to complications during transportation, the animal was not sent to a remote facility to perform a CT scan. Instead, we used a CT scan of the same species provided by the Digital Morphology Museum (PRICT No. 1462, DMM, Tokyo, Japan, downloaded from dmm.pri.kyoto-u.ac.jp/dmm/WebGallery/dicom/dicomProperty.html?id = 1474) as a model of the skull (0.258 mm^3 isotropic resolution, 120 kVp, Toshiba Asteion). CT-images of the skull were registered to the MP-RAGE image using a 3D affine transformation. We used a linear relationship between the Hounsfield Units (HU) from the CT scan and sound speed and density. The power law model for attenuation is $abs = \alpha^* \varphi^\beta$ where the porosity Φ is defined by $\varphi = \frac{\rho_{max} - \rho}{\rho_{max} - \rho_{water}}$ in the skull (Aubry et al., 2003) and absorption coefficient α depends on the frequency: $\alpha = \alpha_0 f^b$.The parameters $\alpha_0 = 8$ dB/cm/MHz^b and $\beta = 0.5$ were determined in a previous work (Constans et al., 2017) by matching simulations with experimental results on a NHP skull flap. b was set to 2 to avoid dispersion (Robertson et al., 2018). This 3D speed of sound map was used as input in the k-wave simulation.

The position of the center of curvature of the transducer as well as its orientation were also required as input parameters. To determine these parameters, the 3D mesh of the water cone was registered to the MP-RAGE acquisition using a landmark registration scheme (Fig. 3). The position of the center of curvature of the transducer was estimated from its focal length (Constans et al., 2017). The location of the acoustic sources were distributed on the corresponding spherical surface in the simulations.

The thermal modeling was based on the bio-heat equation (Pennes, 1948):

$$\rho C \frac{\partial T}{\partial t} = \kappa \nabla^2 T + q + w \rho_b C_b (T - T_a)$$

where T, ρ, C, κ and q are the temperature, density, specific heat, thermal conductivity and rate of heat production respectively. Heat production is defined as $q = \alpha_{abs} \frac{P^2}{2\rho C}$, α_{abs} being the absorption coefficient. According to (Duck, 1990) κ is set to 0.528 W.m-1.K-1 in soft tissue and 0.4 W $m^{-1}.K^{-1}$ in the skull and C is set to 3600 J $kg^{-1}.K^{-1}$ in soft tissue and 1300 J $kg^{-1}.K^{-1}$ in the skull. In the tissue, the absorption coefficient was set to $\alpha_{abs_{tissu}} = 0,13 \frac{dB}{cm}$ at 1 MHz. In the skull the longitudinal absorption coefficient is proportional to the density with $\alpha_{abs_{max}} = \frac{\alpha_0}{3} = \frac{2.7dB}{cm}$ at 1 MHz (Pinton et al., 2012). The last term corresponds to the perfusion process: w, ρ_b, C_b *and* T_a correspond to the blood perfusion rate, blood density, blood specific heat and blood ambient temperature respectively. These parameters were assumed spatially homogeneous over the brain, although a more detailed description of the brain cooling processes can be found in the literature (Wang et al., 2015). The perfusion parameters were taken from Pulkkinen et al. (2011): $w = 0.008 s^{-1}$, $\rho_b = 1030\ kg.m^{-3}$, $C_b = 3620\ J.kg^{-1}K^{-1}$ and $T_a = 37$ °C.

The bioheat equation was solved by using a 3D finite-difference scheme in Matlab (Mathwork, Natick, USA) with Dirichlet boundary conditions. Initial temperature conditions were 37 °C in the brain, skull and tissue, and 24 °C in the water (~5 mm away from the skull).

A viscoelastic model was developed to simulate tissue displacement using the Green functions described by Aki and Richards (2002) for an elastic medium and generalized by Bercoff et al. (2003) for a viscous medium. The displacement induced by a body force distribution f is given by

$$\vec{u}(\vec{r}, t) = \int_\tau d\tau \iiint_V \vec{f}(\vec{\xi}, \tau) \vec{g}(\vec{r} - \vec{\xi}, t - \tau) d\vec{\xi}$$

where g is the Green function (Bercoff et al., 2004).

In this model, the tissue displacement results from the combination of

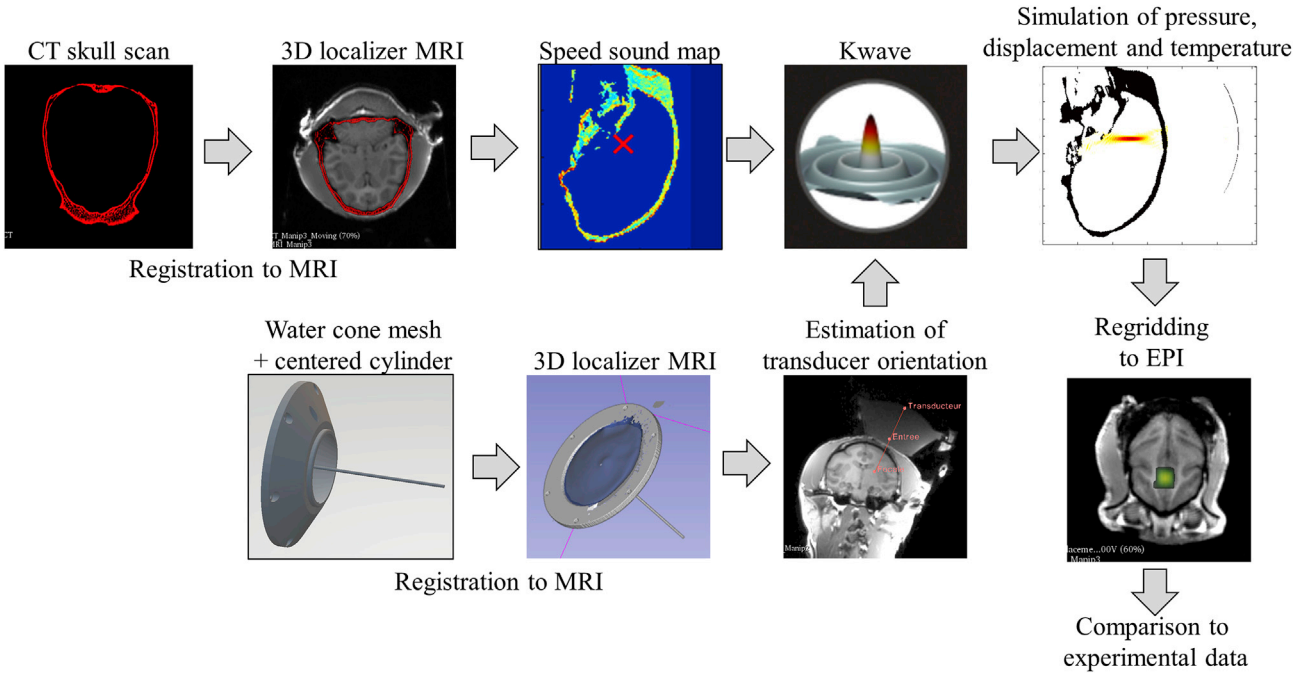

Fig. 3. Protocol of the ultrasound simulation. A CT skull of another NHP brain was registered to the MP-RAGE acquisition. The speed of sound map was extracted from the CT volume. To estimate the center of curvature of the transducer as well as its orientation from the experimental data, the mesh of the water cone was redesigned with a centered cylinder and then registered to the MP-RAGE acquisition. The propagation of focused ultrasound was simulated in an entire NHP head using a k-space pseudospectral method-based solver, k-Wave. Simulation of pressure, displacement and temperature were then computed. Finally, a regridding step was needed to match the EPI orientation and acquisition for comparison to the experimental data.

a compression wave, a shear wave, and a coupling term. Compressional viscosity is assumed to be negligible compared the shear viscosity, as shown by Bercoff et al (Bercoff et al., 2004). The Green function is provided in the annex.

To compute the displacement acquired in MR-ARFI-THERMO sequence, the simulated displacement was integrated over the motion encoding gradient and averaged over time. Finally, simulated data were regridded to match the EPI acquisition and compared to experimental data. Registration and regridding steps were made using 3D Slicer (Fedorov et al., 2012) and ANTs (Avants et al., 2011).

3. Results

Fig. S1 shows the influence of respiration on the accuracy of the displacement estimate in voxels at different locations in the brain (Figs. S1A and S1B). In a slice positioned outside the focus and without respiratory gating, a nearly constant displacement was observed in voxels close to the skull (Fig. S1C). In the slice crossing the focal point (right column), the displacement was visible with a mean ± standard deviation ($\mu_D \pm \sigma_D$) value of 1.2 ± 0.3 µm in the pixel at the focus (Fig. S1D). Important oscillations are visible (Figs. S1E and S1F) in both slices for voxels located deeper into the brain. In respiratory-gated experiments (last column), such oscillations disappeared and resulted in mean ± standard deviation ($\mu_D \pm \sigma_D$) of 0.0 ± 0.2 µm in displacement outside the focus (Fig. S1G) and 0.9 ± 0.2 µm at the focus (Fig. S1H). Values obtained at the same locations without respiratory gating were 0.2 ± 0.3 µm (Fig. S1E) and 1.0 ± 0.7 µm (Fig. S1F), respectively. The resulting refresh rate was 0.36 Hz using gating and 1 Hz without. Residual fluctuations were observed at the focus (Fig. S1H) at t = 20 s and t = 100 s due to imperfect respiratory triggering in this experiment.

Fig. 4 shows a representative result of MR-ARFI-THERMO acquisition (experiment #2, acquisition #4, ARFI in slice direction, $S_{ARFI} = 8$ ms, 279 V, from t = 40 s to t = 80 s) with magnitude, phase, displacement and temperature maps shown at t = 72 s. The temperature maps were overlaid on the magnitude images with a lower threshold value of 0.2 °C. Uniform phase images were observed with a limited presence of phase wraps, illustrating the efficiency of the image reconstruction process. The apparent displacement was visible as a white spot in slices #2 to #4. A temperature increase of 0.4 °C was visible in slice #1 located near the skull. Fig. 4B–C shows temperature and displacement evolution as function of time in a 3 × 3 kernel of voxels at the focus near the focal spot for slices #1 and #3, respectively. Raw measurements can be interpreted without any filtering. A maximum temperature rise of 0.7 °C and a displacement of around 1.5 µm were observed in slice #1 and slice #3, respectively.

Fig. 5A and B shows temporal mean values of displacement (μ_D) and temperature (μ_T) images for each slice of over ten dynamic acquisitions during sonication (from t = 40 s to t = 58 s) and after sonication (from t = 82 s to t = 100 s). Measured values of the temporal mean displacement at the focus were $\mu_D \pm \sigma_D = [1.0 \pm 0.4, 1.5 \pm 0.3, 1.2 \pm 0.6]$ µm in slices #2, #3 and #4 respectively. During sonication, no significant temperature increase could be observed at the focus, whereas an increase was observed after sonication in all slices, with a maximal value of 0.7 °C in slice #1 (closest to the skull). This value was above the standard deviation of temperature which was measured in this experiment below 0.2 °C in the brain for all slices. Fig. 5C shows the orthogonal profiles of displacement measured in slice #3 together with the result of the fit using a 2D Gaussian function (solid lines). A good correspondence with the experimental data was observed with maximal value of 1.2 µm and a FWHM along x and y of 4.8 and 3.8 mm, respectively. Fig. 5D plots the maximal displacement as a function of the applied voltage to the transducer. A quadratic fit was applied because the displacement is proportional to the radiation force (Nightingale et al., 2000) and the radiation force is quadratic with the acoustic pressure amplitude (Rudenko et al., 1996). The fit resulted in $displacement = a.(voltage)^2$, where $a = 3.92.10^{-5}$ µm/V^2.

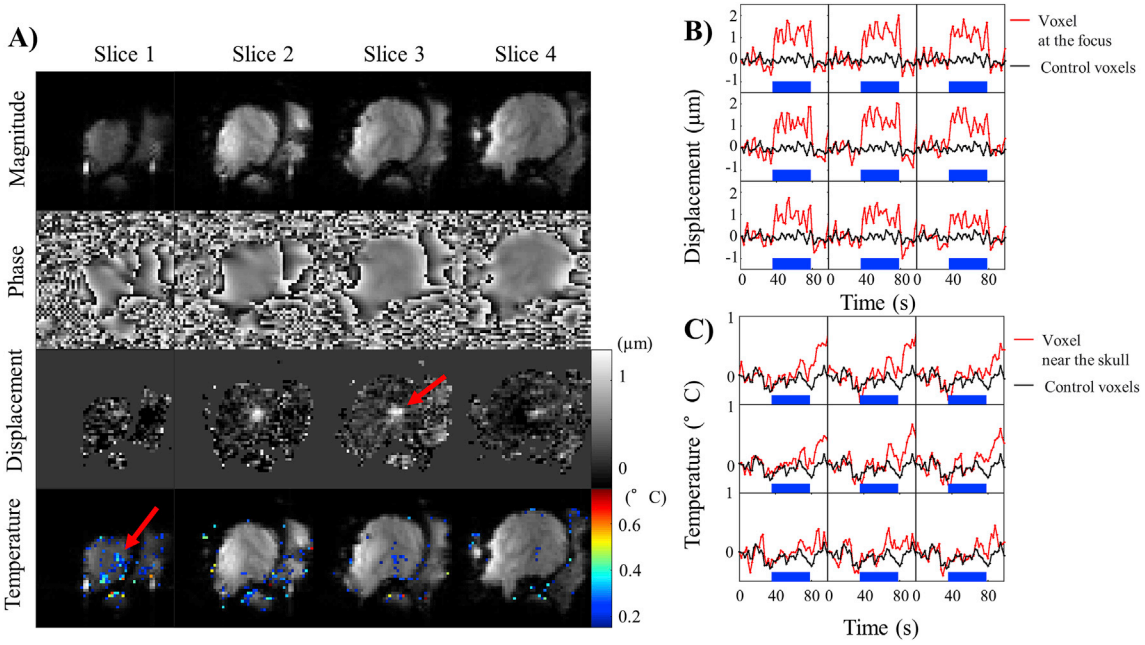

Fig. 4. Displacement and temperature measurements. A) Magnitude and phase images, displacement and temperature maps are shown in four slices at dynamic acquisition n°35 (t = 70 s). For this representative acquisition (acquisition #4, experiment #2, 279 V, $S_{ARFI} = 8$ ms, frame rate = 0.5 Hz), MR slices were oriented perpendicular to the beam direction and ARFI sonication were emitted from dynamic acquisition 20 to 40 (from t = 40 s to t = 80 s). Displacement elevation was clearly visible in slices 2 to 4 (red arrow). Temperature elevation was visible in the first slice (the closest to the skull, red arrow) with a maximum value of 0.7 °C. On the left, displacement (B) and temperature (C) evolution (in red) as function of time are shown in a 3 × 3 kernel of voxels near the focal spot for slices #3 and #1 respectively. The black lines indicate the baseline computed far from the focus location. Physiological noise was recorded in the measurement (tiny oscillation). The temporal mean of the displacement at the focus during the sonication was 1.5 ± 0.3 µm and with a baseline value of -0.1 ± 0.3 µm. Note that temperature increase in the imaging planes occurred at the end of the sonication.

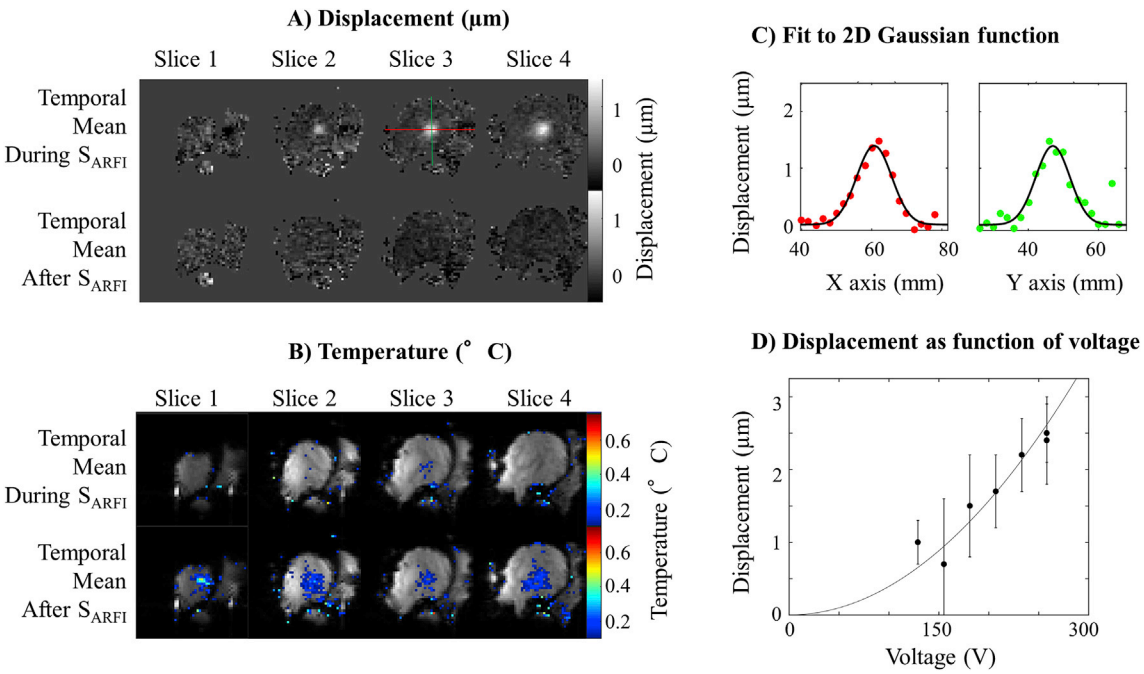

Fig. 5. Mean temporal displacement and temperature measurements. Temporal mean of the displacement (A) and temperature (B) over ten dynamic acquisitions is shown during sonication (from t = 40 s to t = 58 s) and after sonication (from t = 82 s to t = 100 s). HIFU parameters were 279 V, S_{ARFI} = 8 ms, frame rate = 0.5 Hz (acquisition #4, experiment #2). A push was visible in slices #2, #3, #4 with average values of 1.0 ± 0.4, 1.5 ± 0.3, 1.2 ± 0.6 µm respectively. An average temperature increase (0.2 ± 0.1 °C) was monitored in the slices #2 to #4 after the end of the sonication and a larger value was found in slice #1 (0.3 ± 0.2 °C), the closest to the skull. C) Experimental data were fitted to a 2D Gaussian function in order to extract focus location, maximum amplitude and FWHM (results were summarized in Table 1). The displacement profiles along x and y were plotted in red and green and the fitted function in black. D) Seven acquisitions with different peak-to-peak voltage values [129 V, 155 V, 181 V, 207 V, 233 V, 258 V, S_{ARFI} = 4 ms] were acquired. For each acquisition, temporal mean displacement and its standard deviation were fitted to a second order polynomial function Displacement = a*Voltage^2 where a = 3.92e-5 µm/V^2.

Fig. 6 illustrates the results of the simulations for a 279 V driving voltage. The computational domain of the simulation corresponds to the white box displayed in the density map (Fig. 6 Left). The maximum peak negative pressure was 3.59 MPa in the skull and 3.04 MPa in the brain. The maximum tissue displacement was 2.99 µm in the brain.

Fig. 7 compares experimental and simulated displacement at the focus for different applied voltages (from 279 V to 230 V) to the transducer. A consistent spatial correspondence was observed (Fig. 7A), confirmed by spatial profiles plotted in Fig. 7B. The corresponding amplitudes derived from the fit were [1.2, 1.1, 1.0, 0.7] µm and the FWHM along (x, y) were [(4.8, 3.8), (3.7, 4.6), (5.1, 3.6), (4.4, 3.45)] µm, respectively.

Fig. 8 summarize the comparison between simulated and experimental displacement and temperature for a driving voltage of 279 V. Fig. 8C shows simulated temperature (assuming a 37 °C basal temperature) in the skull and brain after the sonication. The maximum simulated temperature was 40.2 °C in the skull, 38.9 °C in the brain and 37.3 °C at the focus. Both experimental and simulated temperature data were temporally filtered and then averaged over five dynamic acquisitions. Results are shown in Fig. 8D (between 46 s and 50 s). The experimental parameters of the thermal maps shown in the figure were: driving voltage = 279 V, S_{ARFI} = 7 ms per slice, frame rate = 1 Hz. Simulated and experimental temperature maps were plotted with a minimum threshold value of 37.01 °C and superimposed on four consecutive anatomical images (Fig. 8D). The largest thermal rise was observed on the first slice (closest to the skull) for both simulated and experimental datasets. At the focus (slices #3 and #4), a 0.2 °C temperature elevation was predicted by the simulation. This was in good agreement with experimental values, since maximal temperature on slices 1 to 4 was [37.9, 37.1, 37.2, 37.2] °C and [39.1, 37.4, 37.4, 37.2] °C for simulated and measured values, respectively. The simulated and raw experimental displacement were overlaid on anatomical images using the same representation in Fig. 8B. Finally Fig. 8A show the maximum pressure amplitude in the sonicated area.

Fig. 9 shows a multiplanar (MPR) rendering from 3DSlicer software of both mean displacement (during sonication) and temperature (after sonication) values superimposed on 3D MP-RAGE images acquired at the beginning of the experiment. The stack of MR-ARFI-THERMO slices is represented by the white rectangle.

Table 1 provides an overview of the experimental results.

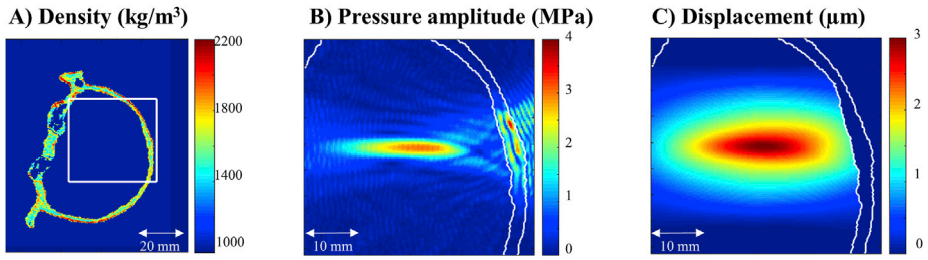

Fig. 6. Simulated displacement. Density map of the NHP head (Left) highlighting the domain of the simulation (white box). The simulated pressure amplitude (Middle) and instantaneous displacement (Right) are shown in a linear scale. The skull contour is displayed in white.

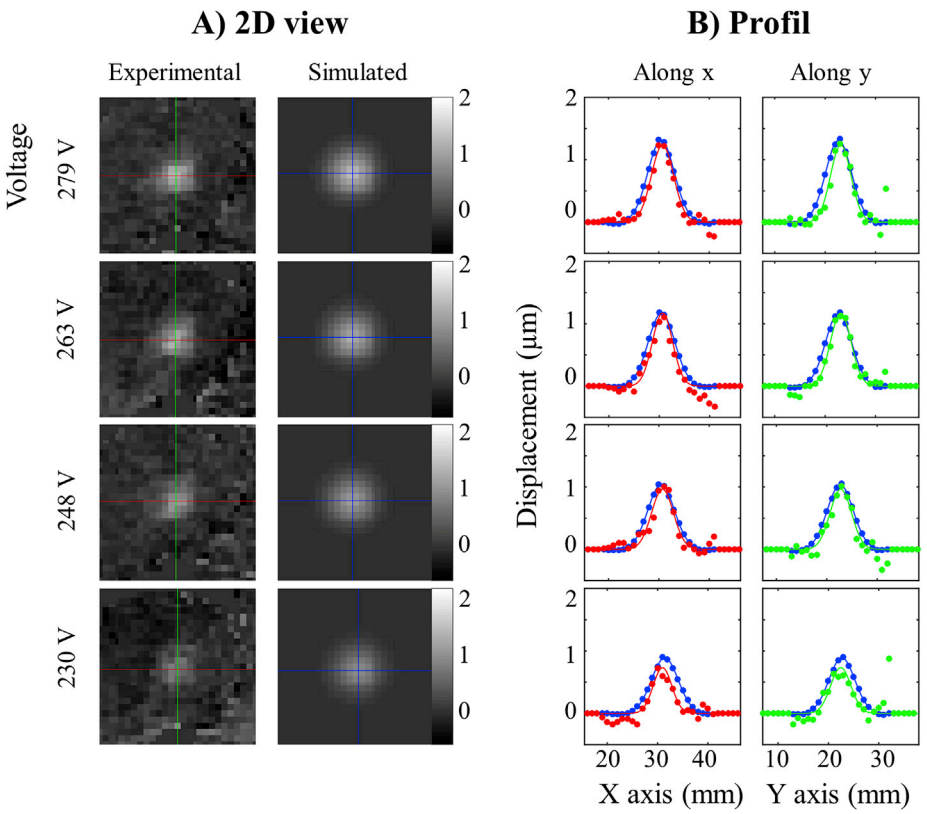

Fig. 7. Comparison between measured and simulated displacement and influence of the peak-to-peak voltage applied to the transducer. In experiment #2, four acquisitions (#9, #10, #11, #12) with different peak-to-peak voltage values [279 V, 263 V, 248 V, 230 V, $S_{ARFI} = 8$ ms per slice] were acquired. The average displacement (the temporal mean of ten dynamic acquisitions during sonication) is shown with two complementary representations of the displacement: A) a 2D view plot of experimental and simulated data, B) a 1D profile along x and y. Measured (red and green) and simulated (blue) data were both fitted to a 2D Gaussian function in order to extract focus location, maximum amplitude and FWHM (see Table 1, experiment 2, acquisition numbers #8 to #11).

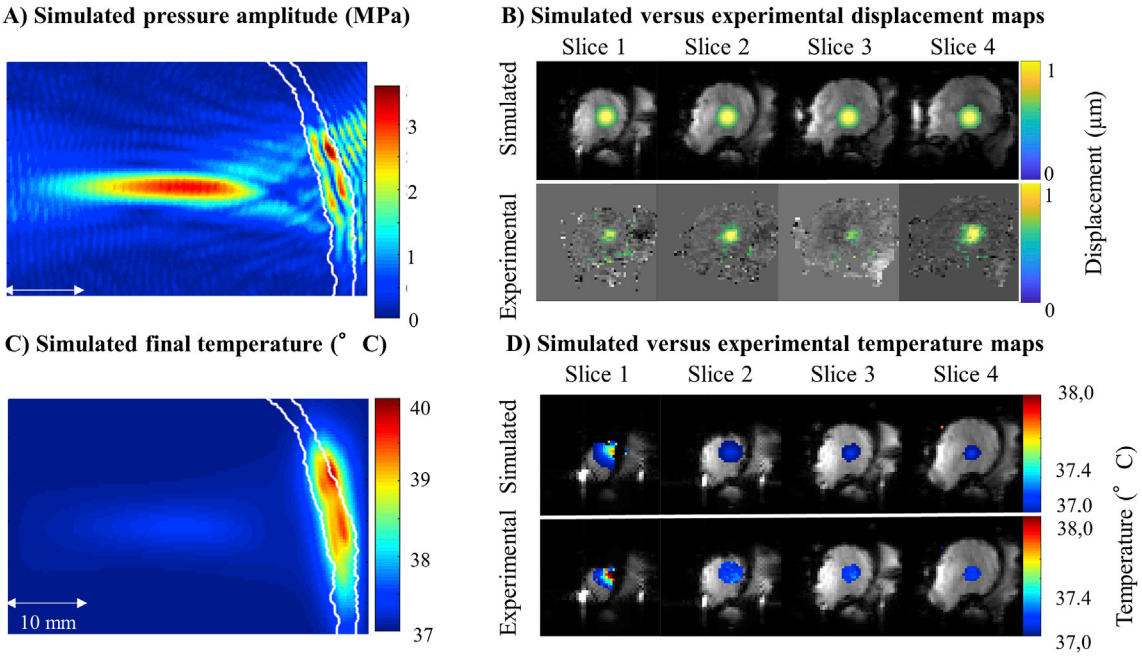

Fig. 8. Comparison between measured and experimental data. A) The simulated pressure amplitude with a linear scale. B) The simulated displacement (top row) overlaid on anatomical images was compared to the average measured displacement (the temporal mean of ten dynamic acquisitions during sonication, bottom row, experiment 2, acquisition #9). C) Map of the simulated maximum temperature in the brain and skull in the sagittal plane of the transducer. D) Simulated (top row) and measured (bottom row) temperature maps superimposed on the anatomical images for four consecutive slices (experiment 2, acquisition #2). Note that the comparison occurs at different location because the simulated displacement were compared to experimental data for different voltage values at the focus to validate the acoustic model with different acoustic radiation pressure, while the temperature data were compared near the skull and in the brain to monitor the energy deposition.

Displacement and temperature measurements were quantified using temporal mean and temporal standard deviation. Over all experiments, the temporal standard deviation of the displacement and of the temperature were about 0.4 µm and 0.2 °C respectively. The temporal mean displacement during sonication ranged between 1 and 2 µm. For each measurement, an estimation of the focal spot dimension was

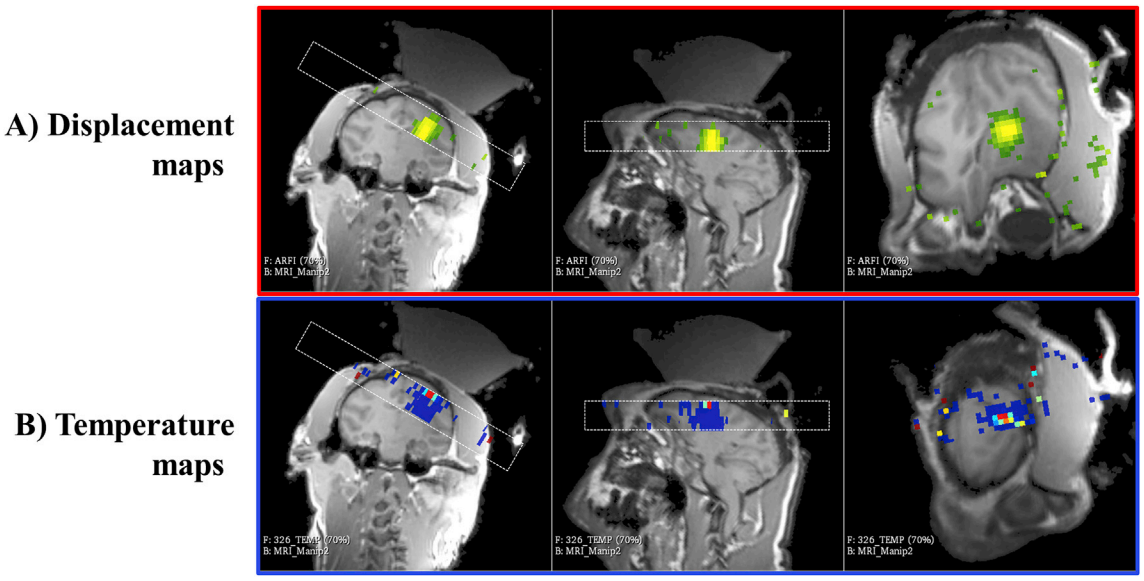

Fig. 9. Visualization of displacement and temperature measurements. MR-ARFI-THERMO acquisition (experiment #2, acquisition #4) was acquired in a plane perpendicular to the beam direction. The position of the stack of EPI slices is indicated by a white rectangle. The temporal mean displacement during sonication (top) and the temporal mean temperature after sonication (below) are overlaid on the image using a gradient color map on the anatomical MP-RAGE acquisition using 3DSlicer software. A (minimum, maximum) value of (0.3, 1.2) μm (top) and of (0.2, 0.5) °C (down) were used as a threshold.

Table 1
Displacement and temperature data. For each acquisition, the temporal standard deviation (σ) and temporal mean (μ) for both displacement (D) and temperature (T) during 10 dynamic acquisitions before (OFF1), during (ON) and after (OFF2) focus ultrasound sonication. Maximum amplitude and FWHM extracted from the 2D Gaussian fit are also indicated.

Acquisition Number	Sonication time (ms)	Voltage (V)	OFF1 (μm) $\mu D \pm \sigma D$	ON (μm) $\mu D \pm \sigma D$	OFF2 (μm) $\mu D \pm \sigma D$	OFF1 (°C) $\mu T \pm \sigma T$	ON (°C) $\mu T \pm \sigma T$	OFF2 (°C) $\mu T \pm \sigma T$	Amplitude (μm)	Width X (mm)	Width Y (mm)	MEG direction
Experiment 1												
1	4	258	-0.1 ± 0.5	1.3 ± 0.4	-0.1 ± 0.5	0.1 ± 0.1	0.2 ± 0.1	0.5 ± 0.2	1.2	6	4.6	slice
2	4	277	-0.2 ± 0.2	1.5 ± 0.2	-0.1 ± 0.3	0.0 ± 0.1	-0.1 ± 0.1	-0.1 ± 0.1	1.3	4.9	3.1	slice
3	4	277	0.1 ± 0.2	1.3 ± 0.5	0.1 ± 0.2	0.0 ± 0.1	0.1 ± 0.1	0.1 ± 0.1	1.3	5.3	3.8	slice
Experiment 2												
1	7	279	0.7 ± 1.6	0.8 ± 1.1	0.3 ± 0.8	-0.2 ± 0.3	-0.1 ± 0.2	-0.0 ± 0.2	1.2	13.1	7.3	phase
2	7	279	-0.1 ± 0.5	1.2 ± 0.5	-0.7 ± 0.5	0.0 ± 0.1	0.0 ± 0.2	0.2 ± 0.1	1.2	4.1	3.1	slice
3	7	279	0.3 ± 0.5	1.5 ± 0.3	0.2 ± 0.3	0.1 ± 0.1	-0.1 ± 0.1	0.0 ± 0.1	1.4	4.3	3.5	slice
4	8	279	-0.1 ± 0.3	1.5 ± 0.3	-0.3 ± 0.6	0.1 ± 0.1	0.0 ± 0.2	0.1 ± 0.1	1.4	4.8	3.9	slice
5	8	279	-0.2 ± 0.3	1.5 ± 0.5	-0.4 ± 0.2	0.0 ± 0.1	0.1 ± 0.2	0.0 ± 0.1	1.4	5.9	5.2	slice
6	8	279	-0.1 ± 0.3	0.8 ± 0.4	0.5 ± 1.0	-0.0 ± 0.1	0.0 ± 0.1	-0.0 ± 0.1	1	8.8	4.2	slice
7	8	279	0.2 ± 0.5	0.8 ± 0.3	0.7 ± 0.6	0.0 ± 0.1	-0.0 ± 0.1	-0.1 ± 0.1	1.1	5	3.1	phase
8	8	279	0.1 ± 0.3	1.1 ± 0.6	0.1 ± 0.2	0.0 ± 0.1	0.1 ± 0.1	0.1 ± 0.0	1.2	12	5.6	phase
9	8	279	-0.2 ± 0.2	1.2 ± 0.2	-0.2 ± 0.4	0.0 ± 0.0	-0.0 ± 0.1	0.0 ± 0.1	1.2	4.8	3.8	phase
10	8	264	0.3 ± 0.2	1.1 ± 0.8	0.4 ± 0.4	-0.0 ± 0.1	0.4 ± 0.1	0.5 ± 0.1	1.2	3.7	4.6	slice
11	8	248	-0.2 ± 0.6	1.0 ± 0.2	-0.2 ± 0.2	0.0 ± 0.1	0.2 ± 0.1	0.4 ± 0.1	1	5.1	3.7	slice
12	8	230	-0.6 ± 0.3	0.6 ± 0.5	-0.6 ± 0.2	0.0 ± 0.1	0.1 ± 0.1	0.0 ± 0.0	0.7	4.4	3.5	slice
Experiment 3												
1	4	258	-0.1 ± 0.5	2.5 ± 0.6	-0.1 ± 0.5	0.2 ± 0.2	0.1 ± 0.2	0.2 ± 0.2	2.2	3.5	3.5	slice
2	4	258	-0.3 ± 0.3	2.4 ± 0.6	-0.3 ± 0.3	0.0 ± 0.1	-0.0 ± 0.2	0.0 ± 0.1	2.5	3.7	3.5	slice
3	4	233	-0.3 ± 0.9	2.2 ± 0.5	-0.3 ± 0.9	0.0 ± 0.2	0.1 ± 0.2	0.0 ± 0.2	1.7	3.3	4.5	slice
4	4	207	-0.2 ± 0.5	1.7 ± 0.5	-0.2 ± 0.5	-0.1 ± 0.3	-0.0 ± 0.3	-0.1 ± 0.3	1.8	3.8	2.7	slice
5	4	181	-0.2 ± 0.6	1.5 ± 0.7	-0.2 ± 0.6	-0.0 ± 0.2	0.2 ± 0.2	-0.0 ± 0.2	1.3	4	5.1	slice
6	4	155	-0.2 ± 0.2	0.7 ± 0.9	-0.2 ± 0.2	0.3 ± 0.2	0.6 ± 0.3	0.3 ± 0.2	-	-	-	slice
7	4	129	-0.1 ± 0.4	1.0 ± 0.3	-0.1 ± 0.4	0.1 ± 0.2	0.4 ± 0.2	0.1 ± 0.2	-	-	-	slice
8	4	258	0.2 ± 0.3	2.5 ± 0.4	0.2 ± 0.3	-0.1 ± 0.1	-0.1 ± 0.1	-0.1 ± 0.1	2.2	3.6	3.1	slice
9	4	258	-0.3 ± 0.4	2.3 ± 0.2	-0.3 ± 0.4	0.0 ± 0.1	0.0 ± 0.1	0.0 ± 0.1	2.2	3	3.2	slice

extracted from the 2D Gaussian fit. FWHM values along x and y ranged between 3 and 5 mm. Although temperature rise in the imaging plane was monitored near the skull, no temperature rise higher than 0.2 °C was measured at the focus, except for acquisitions #10 and #11. Table 2 in the supplementary materials details each acquisition parameter.

4. Discussion

In this work, we exploit a recently published rapid MR-ARFI-THERMO sequence (Bour et al., 2017) for simultaneous real-time imaging of displacement and temperature at 2-mm isotropic resolution in vivo in the brain of NHP during pulsed sonication with a single element

transducer. One goal was to investigate the monitoring capabilities of the sequence under different acoustic power deposition with a transcranial approach. To our knowledge the study presents the first in vivo study of temperature and displacement measurements in NHP, simultaneously providing the ultrasound focal spot location as well as the resulting heating distribution within the brain.

We performed twenty-four MR-ARFI-THERMO measurements in three different experiments. Multiple MR-dynamic acquisitions were acquired and synchronized with sonication during a time window of 10–20 dynamic acquisitions. For each measurement, we computed the uncertainty (temporal standard deviation) and temporal mean value of the measurement before, during and after sonication in order to quantify the uncertainty of the method. Resulting values of $\sigma_T = 0.1\,^{\circ}C$ and $\sigma_D = 0.2\,\mu m$ were found, allowing a clear visualization of measurement change during sonication (see Fig. 5 and S1) where typical displacement of 1.5 μm and temperature change of 1 °C were experimentally observed. The temperature sensitivity is acceptable for thermal applications with typical 20°C thermal rise (Elias et al., 2013), but it also allows to check the potential impact of temperature during TUS experiments, even at low intensities. A 0.5°C thermal rise would correspond, for heat sensitive neurons to a typical 5% increase of firing rate (Bouland, 1974).

MR-ARFI-THERMO was measured either in the slice direction (perpendicular to the beam) or in the phase direction (parallel to the beam). For both situations, we noticed a decrease in precision associated with the presence of strong phase fluctuations when the slices were located at the center of the brain or below. The phase fluctuations turned out to result from magnetic susceptibility changes related to breathing. The sequence was then triggered on the respiratory cycle (0.36 Hz), to minimize the impact of the fluctuations (Fig. S1). This justified the use of a rapid imaging sequence based on a single-shot EPI acquisition with respiratory gating. However, the respiratory-gating acquisition increased the acquisition time (the total acquisition time was about 1 min 20 s for 30 dynamic acquisitions). As an alternative, it should be possible to eliminate the respiratory related phase variation by subtracting the control voxel from the measurement.

A decreasing peak to peak voltage driving the ultrasound transducer was applied to determine the sensitivity threshold value of the method (Fig. 5). In experiment #2, a limited number of acquisitions were available at the same slice position (from 279 V to 230 V, $S_{ARFI} = 8$ ms) allowing a quantification of the displacement amplitude and FWHM. A decrease maximum amplitude from 1.2 μm to 0.7 μm was observed (Table 1). In experiment #3, a new set of acquisitions (from 258 V to 129 V, $S_{ARFI} = 4$ ms) was performed with a reduced sonication duration. A minimum peak to peak voltage of 155 V was necessary to visualize the displacement due to a decrease in signal to noise ratio in this experiment. The results presented in experiment #3 (Table 1) indicate an increased maximum amplitude (2 μm or more at 258 V) in comparison to experiment #2 (1.5 μm at 279 V). This increase in displacement amplitude was attributed to a better positioning of the transducer in experiment #3 (in experiment #2, the transducer was not strictly perpendicular to the skull). In addition, the quality of the acoustic coupling between the water cone and the skin may have impacted the ultrasound transmission to the brain and the focus. In both cases, a relatively sharp displacement was observed with a FHWM between 3 and 5 mm. The peak pressure varied in our study between 1.5 MPa and 3 MPa in water, at 850kHz, with a duration of 4 to 8 ms. This is within the range of typical parameters for brain thermal ablation, with durations of the order of 10 s (Pulkkinen et al., 2014). A wide range of ultrasound parameters have been tested for TUS, with the frequency ranging between 200 kHz and 8 MHz (Naor et al., 2016), the peak pressure from 0.1 MPa to 3.5 MPa and the burst duration between 1 ms and 500 ms (Blackmore and Shrivastava, 2019). Our parameters are thus in the range of thermal ablation and TUS, even though most TUS studies tend to favor low intensity ultrasound, with peak pressure lower than 1.2 MPa. Based on the preliminary results presented here, the displacement could be detected with ARFI for a peak pressure higher than 1.9 MPa at 850 kHz. When using lower peak pressure for TUS, one would have either to improve the sensitivity of the MR-ARFI sequence, or to increase the peak pressure for such sonication MR-ARFI measurement.

A major advantage of single shot EPI is that only one sonication (duration between 4 and 8 ms) per image was required, minimizing the cumulative delivered acoustic energy. In this study, we performed multiple MR dynamic acquisitions to explore the monitoring capabilities of the sequence. For safety reasons, we initially decided to not exploit the minimum acquisition time (300 ms) and used a frame rate of 1 Hz including a dead time of 700 ms. The dead time was increased to 2–3 s during respiratory gated acquisition. 10 to 30 sonication per slice were emitted to potentially visualize induced heat in the brain. The corresponding total sonication time per acquisition ranged from 256 to 672 ms. In the context of focal spot visualization, this value could be drastically reduced, using for example a MR protocol with only 15 dynamics acquisitions (five S_{ARFI}=OFF, five S_{ARFI}=ON, five S_{ARFI}=OFF, with a cumulative sonication time of 100 ms, $S_{total} = 4$ ms x 4 slices x 5). Here, it is worth noting that the sonication parameters used for MR-ARFI may have induced brain neuromodulation if multiple slices were acquired with a high frame rate: neuromodulation was reported with a pulse duration of 5 ms, a stimulus duration of 300 ms and a duty cycle as low as 30% (Kim et al., 2014). Nevertheless, with such parameters, ultrasonic neuromodulation did not last longer than 100 ms (Lee et al., 2016b). Stimulus duration longer than 40 s are needed to induce a sustained effect (Verhagen et al., 2019; Folloni et al., 2019).

The impact of skull and tissue absorption was evaluated with the MR-ARFI-THERMO sequence. Temperature maps were displayed in real-time to monitor temperature elevation. No significant heating effects were noticed but minimal heat deposition (up to 1–2 °C) was observed in the vicinity of the skull. As shown in Fig. 4 and evident in five other acquisitions in experiment #2, the MR-thermometry showed a temperature rise following the sonication. The delay in temperature rise could be explained by the skull absorption of ultrasound energy during sonication. Energy was then transferred to brain tissues in contact with the skull by thermal diffusion. Note that a cooling system was not used in these experiments. Very small temperature increases were observed at the focus during sonication in some experiments, but with temperature increases within the range of the uncertainty of the thermometry method. Further optimization of the sequence parameters may reduce the temperature uncertainty to 0.05 °C or lower.

In the present study, the numerical estimations of temperature and displacements induced by ultrasound have been shown to match with in vivo measurements. Acoustic pressure simulations using the same transducer had been previously validated with pressure fields measurements through a monkey skull (Constans et al., 2017). The thermal modeling was previously used in a retrospective numerical estimation of thermal effect during ultrasonic neurostimulation (Constans et al., 2018), and validated with thermocouple measurements (Constans et al., 2018). In addition to these acoustical and thermal modeling, we used a viscoelastic model to estimate the tissue displacements (Bercoff, 2004). These numerical models were compared to simultaneous measurements if temperature and displacement acquired in the brain of an anesthetized NHP. As can be seen in Fig. 7B, the spatial profiles were in agreement with the experimental values. The maximum temperature at the target location remains below 0.3 °C, which confirms that thermal effects can be neglected at the focal spot during MR-ARFI using such low duty cycle. Our work highlights the occurrence of skull heating (up to 40.2 °C) and the diffusion of the thermal rise to the cortex. In vivo simultaneous measurement of temperature and displacement was a valuable tool to adjust the input parameters of our numerical models. Such models could be useful to design future experimental setup and to estimate the impact of using a given set of ultrasonic parameters.

5. Limitations

As a proof of concept, this study has several limitations. The limited

available experimental time was not sufficient for precisely studying the impact of S_{ARFI} duration on displacement measurements. S_{ARFI} duration = 4 ms was found to be sufficient to monitor displacement. However, shorter value could have been chosen to minimize the sonication duty cycle and the amount of energy delivered to the skull and the brain. The time offset of −2 ms between the beginning of the sonication pulse and second lobe of the MEG may also be refined to further increase the resulting measured displacement at the focus. This was quantitatively studied in a previous work on ex vivo muscle (Bour et al., 2017) and showed a plateau in displacement amplitude after an offset of 2 ms. Nevertheless, the muscle elastic modulus of muscle (2.99 kPa (Lacourpaille et al., 2012)) differs from that normal brain tissue in a closed skull (9.2 kPa (Soza et al., 2005)). Further work could be done to vary the time offset in order to optimize the sensitivity of MR-ARFI for cerebral tissues.

This single shot EPI technique has several potential advantages over multi-shot acquisitions. First, only one sonication is required per slice due to the single readout train acquisition which minimizes heating deposition. Long repetition time can be used to further minimize energy deposition. Second, combined with real-time reconstruction, the sequence acquisition time reduces the treatment planning duration. It provides very fast (30 s) visualization of the focal spot location. However, EPI based sequence are indirectly prone to geometric distortions due to long readout echo trains. Here the echo train length was reduced to 26 ms to reduce such effects. Additional corrections (Dragonu et al., 2009; Jezzard, 2012) and validation should be considered to quantify these effects. Such strategies will require further developments and were considered beyond the scope of the current study.

We show that no substantial heating was observed at the focus under the tested conditions. Thus, MR-ARFI is an excellent way to observe the effect of sonication at the targeted location without inducing unwanted heating. Moderate temperature increase was observed near the skull and may also occur at interfaces between tissues with different acoustic impedances or at the focus using conventional, non-accelerated, MR-ARFI sequences. The proposed combined MR-ARFI-THERMO sequence provides both temperature information and displacement simultaneously using minimal acoustic energy deposition, which is of major interest for safe sonication in the brain.

Although the proposed method is capable of multiple slices acquisition, the volumetric coverage did not cover the entire insonified region. However, additional slices could be acquired with a limited impact on the temporal resolution due to the respiratory gating, at the cost of increased energy deposition. To address this limitation, a simultaneous multi-slice MR-ARFI sequence (Bour et al., 2018) may be developed. Alternatively, sonication may be limited to slices acquired near the expected focal region in order to monitor displacement only where it would be practically useful.

The high temporal and spatial resolution achieved with the proposed MRI techniques may be easily transferred into clinical applications using similar ultrasound setup. Implementation of multi-element receiver coils in existing therapeutic HIFU devices is the only limiting factor for clinical translation of such a monitoring.

In this study, no CT scan of the subject was available. Thus, ultrasound simulations were performed using a CT skull from another Macaca Mulatta, after registration to the MP-RAGE image. This approach does not consider local structural differences between the two skulls, like the skull thickness or the skull surface. Such differences will introduce deviation between simulation and experimental observation.

Finally, the MR-thermometry method does not allow direct measurement of skull heating. However, it can measure radiative temperature increase in brain adjacent to bone. Consequently, the highest temperature in the skull could not be visualized using the PRFS technique and the maximum temperature increase in the brain was reached after the end of sonication. Temperature assessment using T1 (Han et al., 2015) and T2 (Ozhinsky et al., 2016) measurements may help to reduce the risk of overheating.

6. Conclusion

We demonstrate in an alive NHP that simultaneous measurement of thermal rise and displacement is feasible in the brain with a focus ultrasound transcranial approach. The MR-ARFI-THERMO sequence simultaneously provides the ultrasound focal spot location as well as distribution of heating within the brain. Simulations were in good agreement with experimental data and may thus be used for planning the transducer positioning and desired focal spot position in the brain. The current rapid, multi-slice acquisition and real-time implementation of image visualization was compatible with clinical practice and could help to define the operational safety margins for clinical applications of non-invasive transcranial ultrasound brain therapies. The proposed monitoring method has a large applicability in focus ultrasound treatments: 1) prior to treatment, the sequence could improve adaptive focusing procedures by validating the focal location and monitoring (indirectly) the occurrence of skull heating. 2) The sequence could help to differentiate mechanical and thermal effects during ultrasound neurostimulation. 3) The sequence is compatible with a second sonication pulse for thermal ablation energy deposition with high sonication duty cycle (Bour et al., 2017) and could be used during treatment to assess potential tissular modifications during HIFU therapy while showing the temperature distribution in area away from the focus and at the focus.

Ethics approval

The protocol was approved by the local Animal Research Ethics Committee “Darwin” and the “Ministère de l’enseignement supérieur et de la recherche” according to the European rules for animal experimentation (APAFIS ##6355_2016080911065046).

Declaration of competing interestCOI

No other authors have competing interests to declare.

Funding

This work was supported by the Bettencourt Schueller Foundation, the “Agence Nationale de la recherche” under the program “Future Investments’’ with the reference ANR-17-CE19-0007 (CARTLOVE), ANR-10-IAHU-04 (IHU LIRYC), Laboratory of Excellence ANR-10-LABX-57 (TRAIL), ANR-10-EQPX-0015 (Thérapie et Neurostimulation cérébrale de très haute précision par Ultrasons Transcraniens) and ANR-11-INBS-0006 (France Life Imaging, WP3, Phase Brain) and the Inserm ART (Technology Research Accelerator) “Biomedical Ultrasound”.

Authors’ contributions

VO and CC conducted the study, collected the data, analyzed the data and did the primary writing of the manuscript. PB participated to the design and to the optimization of the MR pulse sequence. VO and RV contributed to the design of the image processing pipeline. CC and JFA contributed to the ultrasound modeling. VO, CC, PB, MS, HA, JFA and BQ participated to the experiments. MS, HA, PP, JFA and SL were responsible for the experiments and assisted in the interpretation of the results. VO, JFA and BQ conceived of the study, and participated in its design and coordination. VO, CC, PB, MS, RV, HA, PP, SL, JFA and BQ drafted the manuscript. All authors read and approved the final manuscript.

Acknowledgements

The authors thank John Snell, from the Focused Ultrasound foundation, for proofreading the article.

List of abbreviations

2D	2-dimensional
3D	3-dimensional
ARFI	acoustic radiation force impulse
EPI	Echo Planar Imaging
FA	Flip angle
FOV	Field of view
MEG	motion-sensitive encoding gradient
MR	Magnetic resonance
MRgHIFU	Magnetic resonance guided high intensity focused ultrasound
MRI	Magnetic resonance imaging
NHP	non-human primate
PRFS	Proton resonance frequency shift
SD	standard deviation
TCP/IP	Transmission Control Protocol/Internet
TE	Echo time
TR	Repetition time
TUS	transcranial ultrasonic stimulation

Appendix A. Supplementary data

Supplementary data to this article can be found online at https://doi.org/10.1016/j.neuroimage.2019.116236.

Annex.

$$g_{ij}^{p}(\overrightarrow{r},t) = \frac{1}{4\pi\rho c_p^2}\gamma_i\gamma_j\frac{1}{r}\delta\left(t-\frac{r}{c_p}\right)$$

$$g_{ij}^{s}(\overrightarrow{r},t) = \frac{1}{4\pi\rho c_s}\frac{1}{\sqrt{2\pi\nu_s t}}\frac{\delta_{ij}-\gamma_i\gamma_j}{r}e^{-\frac{\left(t-\frac{r}{c_s}\right)^2 c_s^2}{2\nu_s t}}$$

$$g_{ij}^{ps}(\overrightarrow{r},t) = \frac{1}{4\pi\rho}\left(3\gamma_i\gamma_j-\delta_{ij}\right)\frac{1}{r^3}\left[I_p+I_s\right]$$

where

$$I_p = \frac{\sqrt{\nu_p t}}{\sqrt{2\pi}}\frac{1}{c_p}\left[e^{\frac{-t^2c_p^2}{2\nu_p t}}-e^{\frac{-\left(t-\frac{r}{c_p}\right)^2 c_p^2}{2\nu_p t}}\right]+\frac{t}{2}Erf\left(\frac{c_p t}{\sqrt{2\nu_p t}}\right)-Erf\left(\frac{c_p\left(t-\frac{r}{c_p}\right)}{\sqrt{2\nu_p t}}\right)$$

$$I_s = \frac{\sqrt{\nu_s t}}{\sqrt{2\pi}}\frac{1}{c_s}\left[e^{\frac{-t^2c_s^2}{2\nu_s t}}-e^{\frac{-\left(t-\frac{r}{c_s}\right)^2 c_s^2}{2\nu_s t}}\right]+\frac{t}{2}\left[Erf\left(\frac{c_s t}{\sqrt{2\nu_s t}}\right)-Erf\left(\frac{c_s\left(t-\frac{r}{c_s}\right)}{\sqrt{2\nu_s t}}\right)\right]$$

The body force f induced by ultrasound pressure is given by the following relation: $F(\overrightarrow{r},t)=\frac{2\alpha I(\overrightarrow{r},t)}{c}$ where I is the local intensity of the ultrasound beam $I=\frac{p^2}{2\rho c}$. The convolution was computed in the Fourier space. The parameters were: Young modulus: E = 9.2 kPa (Soza et al., 2005), compressional sound speed: $c_p = 1500$ m/s, shear sound speed: $c_s=\sqrt{\frac{E}{3\rho}}$, shear viscosity = 0.2 Pa s (Bercoff et al., 2004). For the tissue displacement simulation, the grid was interpolated from the original one (dx = 0.258 mm) to a larger one (dx = 0.6 mm) to reduce the memory load.

References

Aki, K., Richards, P.G., 2002. Quantitative Seismology.

Aubry, J.F., Tanter, M., Pernot, M., Thomas, J.L., Fink, M., 2003. Experimental demonstration of noninvasive transskull adaptive focusing based on prior computed tomography scans. J. Acoust. Soc. Am. 113 (1), 84–93. PubMed PMID: 12558249.

Avants, B.B., Tustison, N.J., Song, G., Cook, P.A., Klein, A., Gee, J.C., 2011. A reproducible evaluation of ANTs similarity metric performance in brain image

registration. Neuroimage 54 (3), 2033–2044. https://doi.org/10.1016/j.neuroimage.2010.09.025. PubMed PMID: 20851191; PubMed Central PMCID: PMCPMC3065962.

Bercoff, J.L., 2004. 'imagerie échographique ultrarapide et son application à l'étude de la viscoelasticité du corps humain. ESPCI ParisTECH.

Study of viscous and elastic properties of soft tissues using supersonic shear imaging. In: Bercoff, J., Muller, M., Tanter, M., Fink, M. (Eds.), 2003. IEEE Symposium on Ultrasonics, 2003. IEEE.

Bercoff, J., Tanter, M., Muller, M., Fink, M., 2004. The role of viscosity in the impulse diffraction field of elastic waves induced by the acoustic radiation force. IEEE Trans. Ultrason. Ferroelectr. Freq. Control 51 (11), 1523–1536. PubMed PMID: 15600098.

Bitton, R.R., Pauly, K.R., 2014. MR-acoustic radiation force imaging (MR-ARFI) and susceptibility weighted imaging (SWI) to visualize calcifications in ex vivo swine brain. J. Magn. Reson. Imaging 39 (5), 1294–1300. https://doi.org/10.1002/jmri.24255. PubMed PMID: 24123504; PubMed Central PMCID: PMCPMC3983173.

Blackmore, J., Shrivastava, S., et al., 2019. Ultrasound Neuromodulation: A Review of Results, Mechanisms and Safety. Ultrasound in medicine & biology.

Bouland A., J., et al., 1974. The effect of firing rate on preoptic neuronal thermosensitivity. The Journal of physiology. https://doi.org/10.1113/jphysiol.1974.sp010628.

Bour, P., Marquet, F., Ozenne, V., Toupin, S., Dumont, E., Aubry, J.F., et al., 2017. Real-time monitoring of tissue displacement and temperature changes during MR-guided high intensity focused ultrasound. Magn. Reson. Med. 78 (5), 1911–1921. https://doi.org/10.1002/mrm.26588. PubMed PMID: 28090656.

Bour, P., Ozenne, V., Rapacchi, S., Delcey, M., Schneider, R., Ben Hassen, W., et al. (Eds.), 2018. Volumetric and Rapid MR-Acoustic Radiation Force Imaging Using Simultaneous Multi-Slice Imaging. International Society of Magnetic Resonance in Medicine, Paris.

Constans, C., Deffieux, T., Pouget, P., Tanter, M., Aubry, J.F., 2017. A 200-1380-kHz quadrifrequency focused ultrasound transducer for neurostimulation in rodents and primates: transcranial in vitro calibration and numerical study of the influence of skull cavity. IEEE Trans. Ultrason. Ferroelectr. Freq. Control 64 (4), 717–724. https://doi.org/10.1109/TUFFC.2017.2651648. PubMed PMID: 28092531.

Constans, C., Mateo, P., Tanter, M., Aubry, J.F., 2018. Potential impact of thermal effects during ultrasonic neurostimulation: retrospective numerical estimation of temperature elevation in seven rodent setups. Phys. Med. Biol. 63 (2), 025003 https://doi.org/10.1088/1361-6560/aaa15c. PubMed PMID: 29235453.

Cox, B.T., Kara, S., Arridge, S.R., Beard, P.C., 2007. k-space propagation models for acoustically heterogeneous media: application to biomedical photoacoustics. J. Acoust. Soc. Am. 121 (6), 3453–3464. https://doi.org/10.1121/1.2717409. PubMed PMID: 17552697.

de Bever, J.T., Odeen, H., Hofstetter, L.W., Parker, D.L., 2018. Simultaneous MR thermometry and acoustic radiation force imaging using interleaved acquisition. Magn. Reson. Med. 79 (3), 1515–1524. https://doi.org/10.1002/mrm.26827. PubMed PMID: 28795419; PubMed Central PMCID: PMCPMC5775920.

Deffieux, T., Younan, Y., Wattiez, N., Tanter, M., Pouget, P., Aubry, J.F., 2013. Low-intensity focused ultrasound modulates monkey visuomotor behavior. Curr. Biol. 23 (23), 2430–2433. https://doi.org/10.1016/j.cub.2013.10.029. PubMed PMID: 24239121.

Dragonu, I., de Senneville, B.D., Quesson, B., Moonen, C., Ries, M., 2009. Real-time geometric distortion correction for interventional imaging with echo-planar imaging (EPI). Magn. Reson. Med. 61 (4), 994–1000. https://doi.org/10.1002/mrm.21903. PubMed PMID: 19191281.

Duck, F.A., 1990. Chapter 2 - thermal properties of tissue. In: Duck, F.A. (Ed.), Physical Properties of Tissues. Academic Press, London, pp. 9–42.

Elias, W.J., Khaled, M., Hilliard, J.D., Aubry, J.F., Frysinger, R.C., Sheehan, J.P., et al., 2013. A magnetic resonance imaging, histological, and dose modeling comparison of focused ultrasound, radiofrequency, and Gamma Knife radiosurgery lesions in swine thalamus. J. Neurosurg. 119 (2), 307–317. https://doi.org/10.3171/2013.5.JNS122327. PubMed PMID: 23746105.

Fedorov, A., Beichel, R., Kalpathy-Cramer, J., Finet, J., Fillion-Robin, J.C., Pujol, S., et al., 2012. 3D slicer as an image computing platform for the quantitative imaging network. Magn. Reson. Imaging 30 (9), 1323–1341. https://doi.org/10.1016/j.mri.2012.05.001. PubMed PMID: 22770690; PubMed Central PMCID: PMCPMC3466397.

Folloni, D., Verhagen, L., Mars, R.B., Fouragnan, E., Constans, C., Aubry, J.F., et al., 2019. Manipulation of subcortical and deep cortical activity in the primate brain using transcranial focused ultrasound stimulation. Neuron 101 (6), 1109–1116 e5. https://doi.org/10.1016/j.neuron.2019.01.019. PubMed PMID: 30765166.

In vivo MR-ARFI for transcranial focused ultrasound in large animals. In: Gaur, P., Li, N., Bitton, R., Pauly, K.B. (Eds.), 2018. Joint Annual Meeting of the International Society for Magnetic Resonance in Medicine and the European Society for Magnetic Resonance in Medicine (Paris).

Han, M., Rieke, V., Scott, S.J., Ozhinsky, E., Salgaonkar, V.A., Jones, P.D., et al., 2015. Quantifying temperature-dependent T1 changes in cortical bone using ultrashort echo-time MRI. Magn. Reson. Med. 74 (6), 1548–1555. https://doi.org/10.1002/mrm.25994. PubMed PMID: 26390357; PubMed Central PMCID: PMCPMC4715675.

Hansen, M.S., Sorensen, T.S., 2013. Gadgetron: an open source framework for medical image reconstruction. Magn. Reson. Med. 69 (6), 1768–1776. https://doi.org/10.1002/mrm.24389. PubMed PMID: 22791598.

Hertzberg, Y., Volovick, A., Zur, Y., Medan, Y., Vitek, S., Navon, G., 2010. Ultrasound focusing using magnetic resonance acoustic radiation force imaging: application to ultrasound transcranial therapy. Med. Phys. 37 (6), 2934–2942. https://doi.org/10.1118/1.3395553. PubMed PMID: 20632605.

Huang, Y., Lipsman, N., Schwartz, M.L., Krishna, V., Sammartino, F., Lozano, A.M., et al., 2018. Predicting lesion size by accumulated thermal dose in MR-guided focused ultrasound for essential tremor. Med. Phys. 45 (10), 4704–4710. https://doi.org/10.1002/mp.13126. PubMed PMID: 30098027; PubMed Central PMCID: PMCPMC6181766.

Jeanmonod, D., Werner, B., Morel, A., Michels, L., Zadicario, E., Schiff, G., et al., 2012. Transcranial magnetic resonance imaging-guided focused ultrasound: noninvasive central lateral thalamotomy for chronic neuropathic pain. Neurosurg. Focus 32 (1), E1. https://doi.org/10.3171/2011.10.FOCUS11248. PubMed PMID: 22208894.

Jezzard, P., 2012. Correction of geometric distortion in fMRI data. Neuroimage 62 (2), 648–651. https://doi.org/10.1016/j.neuroimage.2011.09.010. PubMed PMID: 21945795.

Optical tracking-guided MR-ARFI for targeting focused ultrasound neuromodulation in non-human primates. In: Jonathan, S.V., Phipps, M.A., Chaplin, V.L., Singh, A., Yang, P.F., Newton, A.T., et al. (Eds.), 2018. The 18th International Symposium for Therapeutic Ultrasound (Nashville).

Kamimura, H.A., Wang, S., Chen, H., Wang, Q., Aurup, C., Acosta, C., et al., 2016. Focused ultrasound neuromodulation of cortical and subcortical brain structures using 1.9 MHz. Med. Phys. 43 (10), 5730. https://doi.org/10.1118/1.4963208. PubMed PMID: 27782686; PubMed Central PMCID: PMCPMC5045443.

Kaye, E.A., Chen, J., Pauly, K.B., 2011. Rapid MR-ARFI method for focal spot localization during focused ultrasound therapy. Magn. Reson. Med. 65 (3), 738–743. https://doi.org/10.1002/mrm.22662. PubMed PMID: 21337406; PubMed Central PMCID: PMCPMC4099471.

Kim, H., Chiu, A., Lee, S.D., Fischer, K., Yoo, S.S., 2014. Focused ultrasound-mediated non-invasive brain stimulation: examination of sonication parameters. Brain Stimul. 7 (5), 748–756. https://doi.org/10.1016/j.brs.2014.06.011. PubMed PMID: 25088462; PubMed Central PMCID: PMCPMC4167941.

Lacourpaille, L., Hug, F., Bouillard, K., Hogrel, J.Y., Nordez, A., 2012. Supersonic shear imaging provides a reliable measurement of resting muscle shear elastic modulus. Physiol. Meas. 33 (3), N19–N28. https://doi.org/10.1088/0967-3334/33/3/N19. PubMed PMID: 22370174.

Larrat, B., Pernot, M., Aubry, J.-F., Dervishi, E., Sinkus, R., Seilhean, D., et al., 2009. MR-guided transcranial brain HIFU in small animal models. Phys. Med. Biol. 55 (2), 365.

Lee, W., Kim, H.C., Jung, Y., Chung, Y.A., Song, I.U., Lee, J.H., et al., 2016. Transcranial focused ultrasound stimulation of human primary visual cortex. Sci. Rep. 6, 34026. https://doi.org/10.1038/srep34026. PubMed PMID: 27658372; PubMed Central PMCID: PMCPMC5034307.

Lee, W., Lee, S.D., Park, M.Y., Foley, L., Purcell-Estabrook, E., Kim, H., et al., 2016. Image-guided focused ultrasound-mediated regional brain stimulation in sheep. Ultrasound Med. Biol. 42 (2), 459–470. https://doi.org/10.1016/j.ultrasmedbio.2015.10.001. PubMed PMID: 26525652.

Legon, W., Sato, T.F., Opitz, A., Mueller, J., Barbour, A., Williams, A., et al., 2014. Transcranial focused ultrasound modulates the activity of primary somatosensory cortex in humans. Nat. Neurosci. 17 (2), 322–329. https://doi.org/10.1038/nn.3620. PubMed PMID: 24413698.

Lipsman, N., Schwartz, M.L., Huang, Y., Lee, L., Sankar, T., Chapman, M., et al., 2013. MR-guided focused ultrasound thalamotomy for essential tremor: a proof-of-concept study. Lancet Neurol. 12 (5), 462–468. https://doi.org/10.1016/S1474-4422(13)70048-6. PubMed PMID: 23523144.

Lipsman, N., Meng, Y., Bethune, A.J., Huang, Y., Lam, B., Masellis, M., et al., 2018. Blood-brain barrier opening in Alzheimer's disease using MR-guided focused ultrasound. Nat. Commun. 9 (1), 2336. https://doi.org/10.1038/s41467-018-04529-6. PubMed PMID: 30046032; PubMed Central PMCID: PMCPMC6060168.

Marsac, L., Chauvet, D., Larrat, B., Pernot, M., Robert, B., Fink, M., et al., 2012. MR-guided adaptive focusing of therapeutic ultrasound beams in the human head. Med. Phys. 39 (2), 1141–1149. https://doi.org/10.1118/1.3678988. PubMed PMID: 22320825; PubMed Central PMCID: PMCPMC3432021.

Martinez-Fernandez, R., Rodriguez-Rojas, R., Del Alamo, M., Hernandez-Fernandez, F., Pineda-Pardo, J.A., Dileone, M., et al., 2018. Focused ultrasound subthalamotomy in patients with asymmetric Parkinson's disease: a pilot study. Lancet Neurol. 17 (1), 54–63. https://doi.org/10.1016/S1474-4422(17)30403-9. PubMed PMID: 29203153.

Mougenot, C., Waspe, A., Looi, T., Drake, J.M., 2016. Variable ultrasound trigger delay for improved magnetic resonance acoustic radiation force imaging. Phys. Med. Biol. 61 (2), 712–727. https://doi.org/10.1088/0031-9155/61/2/712. PubMed PMID: 26717008.

Naor, O., Krupa, S., Shoham, S., 2016. Ultrasonic neuromodulation. J. Neural Eng. 13 (3), 031003 https://doi.org/10.1088/1741-2560/13/3/031003. PubMed PMID: 27153566.

Nightingale, K.R., Nightingale, R.W., Palmeri, M.L., Trahey, G.E., 2000. A finite element model of remote palpation of breast lesions using radiation force: factors affecting tissue displacement. Ultrason. Imaging 22 (1), 35–54.

Odeen, H., de Bever, J., Hofstetter, L.W., Parker, D.L., 2018. Multiple-point magnetic resonance acoustic radiation force imaging. Magn. Reson. Med. https://doi.org/10.1002/mrm.27477. PubMed PMID: 30257059.

Ozhinsky, E., Han, M., Bucknor, M., Krug, R., Rieke, V., 2016. T2-based temperature monitoring in bone marrow for MR-guided focused ultrasound. J Ther. Ultrasound 4, 26. https://doi.org/10.1186/s40349-016-0073-8. PubMed PMID: 27882240; PubMed Central PMCID: PMCPMC5112680.

Paquin, R., Vignaud, A., Marsac, L., Younan, Y., Lehericy, S., Tanter, M., et al., 2013. Keyhole acceleration for magnetic resonance acoustic radiation force imaging (MR ARFI). Magn. Reson. Imaging 31 (10), 1695–1703. https://doi.org/10.1016/j.mri.2013.07.011. PubMed PMID: 24079934.

Pennes, H.H., 1948. Analysis of tissue and arterial blood temperatures in the resting human forearm. J. Appl. Physiol. 1 (2), 93–122. PubMed PMID: 18887578.

Peters, R.D., Hinks, R.S., Henkelman, R.M., 1998. Ex vivo tissue-type independence in proton-resonance frequency shift MR thermometry. Magn. Reson. Med. 40 (3), 454–459. PubMed PMID: 9727949.

Pinton, G., Aubry, J.F., Bossy, E., Muller, M., Pernot, M., Tanter, M., 2012. Attenuation, scattering, and absorption of ultrasound in the skull bone. Med. Phys. 39 (1), 299–307. https://doi.org/10.1118/1.3668316. PubMed PMID: 22225300.

Plaksin, M., Shoham, S., Kimmel, E., 2014. Intramembrane cavitation as a predictive bio-piezoelectric mechanism for ultrasonic brain stimulation. Phys. Rev. X 4 (1). https://doi.org/10.1103/PhysRevX.4.011004, 011004.

Pulkkinen, A., Huang, Y., Song, J., Hynynen, K., 2011. Simulations and measurements of transcranial low-frequency ultrasound therapy: skull-base heating and effective area of treatment. Phys. Med. Biol. 56 (15), 4661–4683. https://doi.org/10.1088/0031-9155/56/15/003. PubMed PMID: 21734333.

Pulkkinen, A., Werner, B., Martin, E., Hynynen, K., et al., 2014. Numerical simulations of clinical focused ultrasound functional neurosurgery. Physics in Medicine & Biology.

Robertson, J., Urban, J., Stitzel, J., Treeby, B.E., 2018. The effects of image homogenisation on simulated transcranial ultrasound propagation. Phys. Med. Biol. 63 (14), 145014. https://doi.org/10.1088/1361-6560/aacc33. PubMed PMID: 29897047.

Rudenko, O., Sarvazyan, A., Emelianov, S.Y., 1996. Acoustic radiation force and streaming induced by focused nonlinear ultrasound in a dissipative medium. J. Acoust. Soc. Am. 99 (5), 2791–2798.

Soza, G., Grosso, R., Nimsky, C., Hastreiter, P., Fahlbusch, R., Greiner, G., 2005. Determination of the elasticity parameters of brain tissue with combined simulation and registration. Int. J. Med. Robot. 1 (3), 87–95. https://doi.org/10.1002/rcs.32. PubMed PMID: 17518395.

Tufail, Y., Yoshihiro, A., Pati, S., Li, M.M., Tyler, W.J., 2011. Ultrasonic neuromodulation by brain stimulation with transcranial ultrasound. Nat. Protoc. 6 (9), 1453–1470. https://doi.org/10.1038/nprot.2011.371. PubMed PMID: 21886108.

Verhagen, L., Gallea, C., Folloni, D., Constans, C., Jensen, D.E., Ahnine, H., et al., 2019. Offline impact of transcranial focused ultrasound on cortical activation in primates. Elife 8. https://doi.org/10.7554/eLife.40541. PubMed PMID: 30747105; PubMed Central PMCID: PMCPMC6372282.

Wang, H., Kim, M., Normoyle, K.P., Llano, D., 2015. Thermal regulation of the brain-an anatomical and physiological review for clinical neuroscientists. Front. Neurosci. 9, 528. https://doi.org/10.3389/fnins.2015.00528. PubMed PMID: 26834552; PubMed Central PMCID: PMCPMC4720747.

Wattiez, N., Constans, C., Deffieux, T., Daye, P.M., Tanter, M., Aubry, J.F., et al., 2017. Transcranial ultrasonic stimulation modulates single-neuron discharge in macaques performing an antisaccade task. Brain Stimul. 10 (6), 1024–1031. https://doi.org/10.1016/j.brs.2017.07.007. PubMed PMID: 28789857.

Yang, P.S., Kim, H., Lee, W., Bohlke, M., Park, S., Maher, T.J., et al., 2012. Transcranial focused ultrasound to the thalamus is associated with reduced extracellular GABA levels in rats. Neuropsychobiology 65 (3), 153–160. https://doi.org/10.1159/000336001. PubMed PMID: 22378299.

Ye, P.P., Brown, J.R., Pauly, K.B., 2016. Frequency dependence of ultrasound neurostimulation in the mouse brain. Ultrasound Med. Biol. 42 (7), 1512–1530. https://doi.org/10.1016/j.ultrasmedbio.2016.02.012. PubMed PMID: 27090861; PubMed Central PMCID: PMCPMC4899295.

Younan, Y., Deffieux, T., Larrat, B., Fink, M., Tanter, M., Aubry, J.F., 2013. Influence of the pressure field distribution in transcranial ultrasonic neurostimulation. Med. Phys. 40 (8), 082902 https://doi.org/10.1118/1.4812423. PubMed PMID: 23927357.

Zheng, Y., Marx, M., Miller, G.W., Butts Pauly, K., 2018. High sensitivity MR acoustic radiation force imaging using transition band balanced steady-state free precession. Magn. Reson. Med. 79 (3), 1532–1537. https://doi.org/10.1002/mrm.26793. PubMed PMID: 28631853; PubMed Central PMCID: PMCPMC5995567.